Lab on a Chip

PAPER

View Article Online
View Journal | View Issue

Cite this: *Lab Chip*, 2021, **21**, 2738

Label-free inertial-ferrohydrodynamic cell separation with high throughput and resolution†

Yang Liu, [a] Wujun Zhao,[e] Rui Cheng,[b] Alicia Puig,[c] Jamie Hodgson,[d] Mary Egan,[d] Christen N. Cooper Pope,[d] Petros G. Nikolinakos[d] and Leidong Mao *[b]

Received 2nd April 2021,
Accepted 7th May 2021

DOI: 10.1039/d1lc00282a

rsc.li/loc

Rapid and label-free separation of target cells from biological samples provided unique opportunity for disease diagnostics and treatment. However, even with advanced technologies for cell separation, the limited throughput, high cost and low separation resolution still prevented their utility in separating cells with well-defined physical features from a large volume of biological samples. Here we described an ultrahigh-throughput microfluidic technology, termed as inertial-ferrohydrodynamic cell separation (inertial-FCS), that rapidly sorted through over 60 milliliters of samples at a throughput of 100 000 cells per second in a label-free manner, differentiating the cells based on their physical diameter difference with ~1–2 μm separation resolution. Through the integration of inertial focusing and ferrohydrodynamic separation, we demonstrated that the resulting inertial-FCS devices could separate viable and expandable circulating tumor cells from cancer patients' blood with a high recovery rate and high purity. We also showed that the devices could enrich lymphocytes directly from white blood cells based on their physical morphology without any labeling steps. This label-free method could address the needs of high throughput and high resolution cell separation in circulating tumor cell research and adoptive cell transfer immunotherapy.

Introduction

High-throughput and high-resolution separation of target cells in a label-free manner from a large volume of biological samples has increasingly found applications in both fundamental biological research and clinical assays.[1–3] These target cells can harbor important information about diseases such as in the case of rare circulating tumor cells (CTCs) and metastatic cancers[4–9] or can be candidates for potent therapeutic cells, such as in the case of T lymphocytes in cancer immunotherapies.[10–12] For example, CTCs, cancer cells that are detached from primary tumors and carried through the vasculature to potentially seed distant site metastases in vital organs, have significant implications in cancer research and clinical utility of diagnosing and treating cancer.[4–9] However, one major bottleneck of CTC research has been the limited availability of CTCs for investigations, due to their rarity as well as physical and biological heterogeneities in blood circulation, which typically yields only 1–10 CTCs from one milliliter of human whole blood. The scarcity and heterogeneity of CTCs highlighted a need for new cell separation methods that could quickly enrich CTCs from a large quantity of contaminating blood cells (~10^7–10^8 white blood cells) in a clinically relevant amount of blood (~10 milliliters). Another area that could potentially benefit from high-throughput and high-resolution cell separation is adoptive cell transfer (ACT) immunotherapy, in which T lymphocytes are purified, genetically modified and infused into cancer patients to mediate anti-tumor effects.[10–12] One major bottleneck and a significant contributor to the high price point of ACT is the cost associated with the purification of T lymphocytes from concentrated samples of human blood cells, which consist of ~10^9 white blood cells (WBCs) and other blood components including platelets and red blood cells.[13] In order to derive potent therapeutic cells in ACT, high-purity T lymphocyte separation from WBCs became critical, which in turn necessitated the development of high-throughput and high-resolution cell separation methods that could enrich large quantities of T lymphocytes from concentrated WBCs in a low-cost manner.

The current cell separation platforms have not met the needs of the above-mentioned applications because they faced challenges including high cost, low separation resolution and limited sample processing volume. Traditionally, target cells are separated from contaminating cells using methods including magnetic-activated cell sorting

[a] *Department of Chemistry, The University of Georgia, Athens, Georgia, USA*
[b] *School of Electrical and Computer Engineering, College of Engineering, The University of Georgia, Athens, Georgia, USA. E-mail: mao@uga.edu*
[c] *Department of Microbiology, Texas State University, San Marcos, Texas, USA*
[d] *University Cancer & Blood Center, LLC, Athens, Georgia, USA*
[e] *FCS Technology LLC, Athens, Georgia, USA*

† Electronic supplementary information (ESI) available. See DOI: 10.1039/d1lc00282a

(MACS) or fluorescence-activated cell sorting (FACS). MACS is a label-based method that relies on the interaction between magnetic beads and surface antigens of target or contaminating cells.[14] This method has high cost due to the use of expensive antibodies and magnetic beads. On the other hand, the throughput of the FACS method is limited to $\sim 10^3$ cells per second,[15] far below the needed throughput ($\sim 10^5$ cells per second) in CTC or T lymphocyte separation. The majority of existing microfluidic cell separation methods, despite their precision, also suffered from low throughput as they typically were limited to processing a small amount of biological sample in the range of microliters to a few milliliters (see the ESI† for comparison).[16–21] The exception was the recently developed inertial force-based microfluidic systems, which resulted in focusing and separation of biological particles based on their size difference with extremely high throughput ($\sim 10^5$ cells per second) but relatively low resolution.[22–27] These challenges in the current methods highlighted an urgent need to develop a high-throughput and high resolution method that can separate target cells from a large volume of biological samples in a low-cost manner.

To address this need, we developed a label-free inertial-ferrohydrodynamic cell separation (inertial-FCS) method that was based on the integration of inertial focusing and ferrohydrodynamic separation of cells according to their physical diameters. This method could separate target cells from contaminating cells with a high throughput of $\sim 10^5$ cells per second, a high sample processing flow rate of $\sim$60 mL h^{-1} and a high separation resolution of $\sim$1–2 μm in cellular diameter difference. Due to its label-free nature, this method didn't require the use of antibodies and magnetic beads and could lower the cost of cell separation. In this paper, we presented the working principle of the inertial-ferrohydrodynamic cell separation (inertial-FCS) method, the design and optimization of its associated device for high-throughput and high-resolution cell separation, and the validation of the device using spiked cancer cells, blood samples from cancer patients, and human white blood cells.

Results and discussion

Overview of inertial-ferrohydrodynamic cell separation

The underlying working principle of inertial-ferrohydrodynamic cell separation (inertial-FCS) is the integration of the inertial focusing and ferrohydrodynamic separation of cells of interest based on their physical diameters (Fig. 1a). In order to achieve high throughput and high resolution separation of cells, we first used an inertial focusing principle to order cells into narrow streams in sigmoidal microchannels with alternating curvatures in the first stage of the inertial-FCS device (Fig. 1a). Cells were inertially focused prior to their separation. In this stage, the channel Reynolds number (R_c) was estimated to be 68.3, and the particle Reynolds number (R_p) was 1.3 when the sample flow rate was 60 mL h^{-1} (see the ESI† for the Reynolds number calculation). The combination of the channel design and flow parameters in this stage enabled the cells in the sample to experience both inertial lift and Dean drag forces that forced them to migrate to balanced locations within the curved channel in the first stage (Fig. 1c).[28–30] In the second stage of the device, we ferrohydrodynamically separated the inertially focused cell streams into different spatial locations based on the physical diameters of the cells. The principle of ferrohydrodynamic cell separation in a biocompatible ferrofluid is illustrated in Fig. 1b. Cells immersed in a custom-made biocompatible ferrofluid, which is a uniformly magnetic medium consisting of colloidally stable maghemite nanoparticles, possessed an induced imaginary magnetic dipole moment in a non-uniform magnetic field, which in turn generated a cell volume-dependent magnetic body force, also referred to as magnetic buoyancy force that drove the cells away from the magnetic field maxima.[31–36] Forces on the cells can therefore separate them based on their physical diameters in a continuous ferrofluid flow. Through the integration of both inertial focusing and ferrohydrodynamic separation, we later achieved a high sample flow rate ($\sim$60 mL h^{-1}) and a high cell processing throughput ($\sim 10^5$ cells per s) while being able to differentiate cells with a diameter difference of $\sim$1–2 μm in two separate validations.

Optimization of inertial-ferrohydrodynamic cell separation

We first optimized the inertial-ferrohydrodynamic cell separation (inertial-FCS) device for high cell-processing throughput separation of target cells. The throughput performance targets of the inertial-FCS device in cell separation included: (1) a cell-processing throughput of $\sim 10^5$ cells per second and a sample processing flow rate of >60 mL per hour, and (2) a high recovery rate and purity of separated cells. These performance metrics were chosen after considering the separation requirements of the samples that contained cancer cells or lymphocytes, as well as the challenges faced by the existing cell separation methods (see the ESI†).[16–27]

Systematic optimization of high-throughput inertial-FCS devices focused on the effects of the device geometry, magnetic field and its gradient, sample flow rates, and ferrofluid concentration on the device performance, including the cell-processing throughput, recovery rate and purity of separated cells. This optimization was conducted using a previously developed physical model that took into consideration the balanced magnetic buoyance force and hydrodynamic viscous force on cells under laminar flow conditions.[37,38] Firstly, we determined the microchannel dimensions for both inertial focusing and ferrohydrodynamic separation stages by balancing the need to process at least 60 milliliters of samples within one hour and the need to achieve inertial focusing of cells in the sigmoidal microchannels with alternating curvatures. The inertial focusing channel dimensions were optimized so that the channel Reynolds number (R_c) was 63.8 and the particle

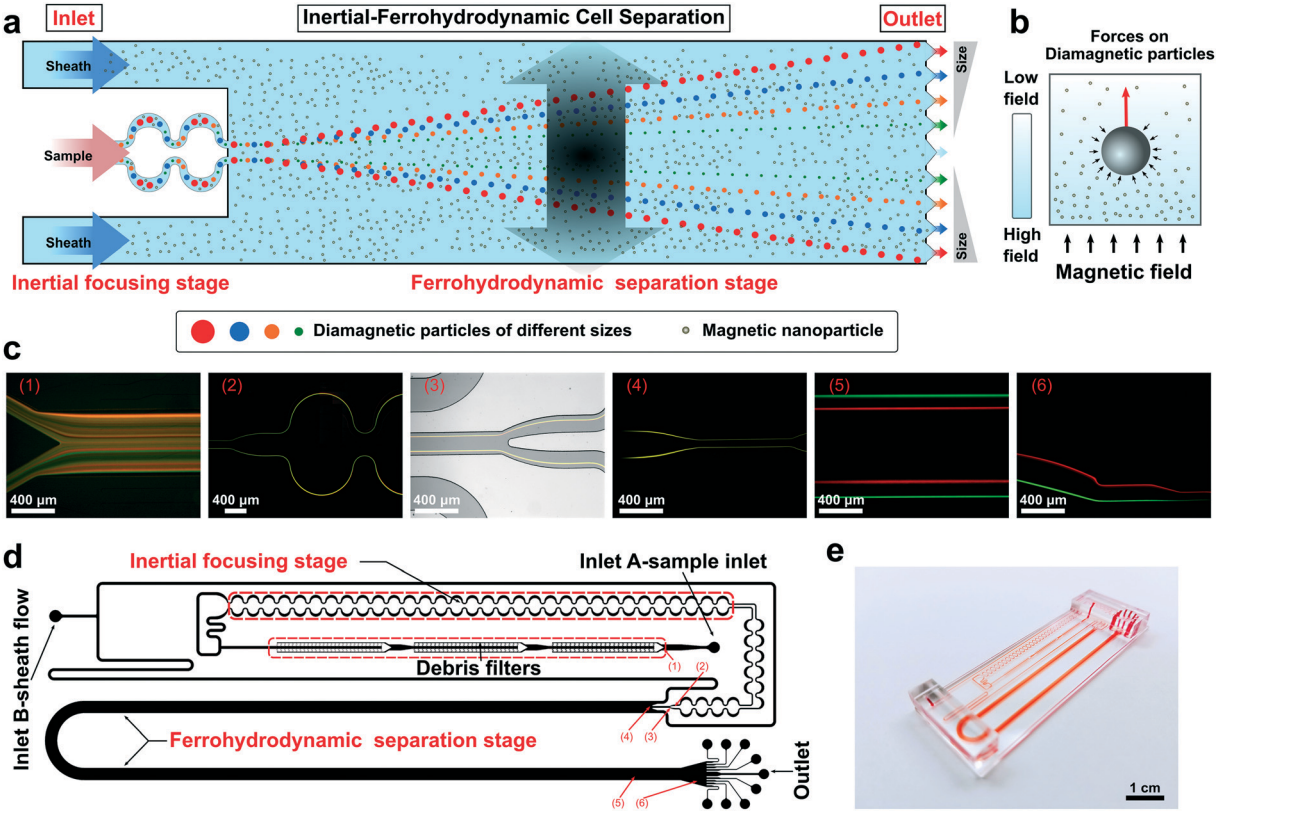

Fig. 1 Overview of the inertial-ferrohydrodynamic cell separation (inertial-FCS) scheme and its device. (a) Working principle of the inertial-FCS. Cells within a custom-made biocompatible ferrofluid were inertially focused into a narrow stream in curved microchannels in the first stage of the device (inertial focusing stage). This cell stream was then ferrohydrodynamically separated into multiple streams according to the cells' physical diameter in the second stage of the device (ferrohydrodynamic separation stage). The black arrow with gradient indicates the distribution of the magnetic field in the microchannel. (b) Schematic of a diamagnetic particle experiencing ferrohydrodynamic force in a colloidally-stable magnetic nanoparticle suspension (*i.e.,* ferrofluids). The magnetization of the diamagnetic particle was near zero and much less than that of its surrounding ferrofluid. The ferrohydrodynamic force on the diamagnetic particles was generated from the pressure *via* nanoparticle collisions on the particle's surface, which was proportional to the particle volume, the magnetization of the ferrofluid, and the gradient of the magnetic field strength. The color bar indicates the relative amplitude of the magnetic field strength. The red arrow shows the direction of the ferrohydrodynamic force that points away from the stronger magnetic field, and the small black arrows on the diamagnetic particle surface show the direction of interaction between magnetic nanoparticles and the diamagnetic particle. (c) Images of the inertial-FCS channel in operation. Red (6 μm in diameter) and green (10 μm in diameter) polystyrene beads were mixed in a ferrofluid and injected into the device to obtain these images. (1) Particles prior to inertial focusing. (2–4) Particles after inertial focusing but before ferrohydrodynamic separation. (5–6) Particles after ferrohydrodynamic separation. The sample flow rate was 600 μL min^{-1}. (d) Top-view schematic drawing of the inertial-FCS device channel. Cells were injected into the channel from inlet A. After going through a debris filter that removed large debris, cells were inertially focused in curved channels (labeled the inertial focusing stage). The sheath flow was injected into inlet B to further narrow the sample stream and control the starting points of cells. Cells were then ferrohydrodynamically separated based on their physical diameter. Separated cells were collected from the outlets for further analysis. (e) A photo of the inertial-FCS microchannel.

Reynolds number (R_p) was 1.3 when the flow rate was 1000 μL min^{-1} or 60 mL h^{-1}, ensuring that the cells would experience inertial focusing and self-organize into narrow streams prior to the separation.[28] The schematic and prototype microchannel of an inertial-FCS device are shown in Fig. 1d and e. Secondly, we optimized the generation of an external magnetic field gradient because the amplitude of magnetic force on cells was proportional to the amplitude of the magnetic field gradient.[31–36] In order to maximize the field gradient, we adopted a sextupole magnet configuration in the inertial-FCS device that could generate a magnetic flux density in the range of 0–3.2 T (1.1–1.3 T within the separation microchannel) and a magnetic flux density gradient of up to 670 T m^{-1} (Fig. 2a). The microchannel and the sextupole magnets were placed in such a way that the magnetic flux density was highest at the center of the channel in the *y*-direction (see Fig. 2 for coordinates) and had a symmetric distribution (Fig. 2b). The purpose of such a configuration was to ferrohydrodynamically drive the inertially focused cells away from the center of the channel (*y*-direction) for diameter-dependent spatial separation. The migration distance of the cells in the *y*-direction depended on their physical diameter: cells with a larger diameter migrated more, leading to spatial separation of cells (Fig. 2c).

The remaining optimization focused on the effect of the ferrofluid concentration (volumetric fraction of magnetic

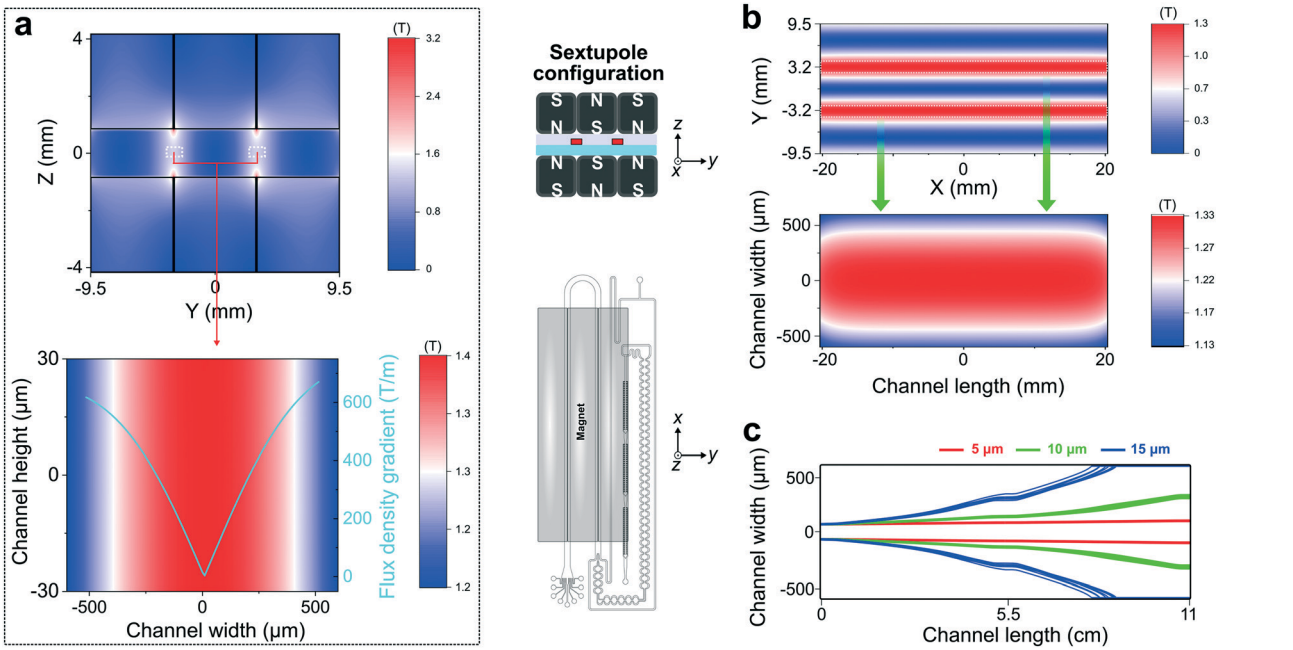

Fig. 2 Magnetic field optimization of the inertial-FCS device. (a) The sextupole magnet configuration in the inertial-FCS device generated a high magnetic flux density and its gradient sufficient for cell separation. Using six permanent magnets (50.8 mm by 6.35 mm by 6.35 mm, N52 neodymium magnet) in a sextupole configuration shown here (top panel), a magnetic flux density of up to 1.4 T in the *y*–*z* plane (x = 0) and a magnetic flux density gradient of >600 T m^{-1} in the *y*–*z* plane (x = 0) were generated (bottom panel). The dashed white lines in the top panel indicate the locations of the separation microchannel. The configuration of the magnets and the microchannel is shown here. (b) The distribution of the magnetic flux density in the separation microchannel. The highest magnetic flux density is located at the center of the microchannel in the *x*–*y* plane (z = 0), and the distribution of the flux density is symmetric in the channel in the *y*-direction. This was chosen so that the cells in the channel would be driven ferrohydrodynamically from the center to the sides of the channel based on their physical diameter. The dashed white lines in the top panel indicate the locations of the separation microchannel. (c) Simulated particle (5 μm, 10 μm, and 15 μm diameter polystyrene beads) trajectories in the inertial-FCS device in the *x*–*y* plane show that these particles could be separated based on their diameters. The sample flow rate was 1000 μL min^{-1}.

materials in the ferrofluid) and cell-processing sample flow rate on the performance of the ferrohydrodynamic separation stage. For this part of optimization, we calculated an output – a separation distance in the *y*-direction (see Fig. 2 for coordinates) between cells with different diameters, denoted as ΔY. ΔY was optimized using parameters including the ferrofluid concentration (0–0.3% v/v) and sample flow rate (100–1200 μL min^{-1}, *i.e.*, 6–72 mL h^{-1}). The goal was to maximize the separation distance while achieving the highest sample flow rate simultaneously. We first optimized the flow ratio between the sample flow and the sheath flow to be 2 when the sample flow rate was 600–1200 μL min^{-1} through simulation (Fig. 3a). This optimized flow ratio allowed us to control the locations of the cells immediately after their inertial focusing so that maximal separation between the cells could be achieved (see the ESI†). We then determined the dependence of the separation distance ΔY on the ferrofluid concentration and the sample flow rate as shown in Fig. 3b and c through both simulations and experiments. The simulation results showed that for a specific sample flow rate, there existed a corresponding optimal ferrofluid concentration that led to a maximal separation distance between the cells. We experimentally verified this dependence in Fig. 3d and e using a mixture of 6 μm and 10 μm (diameters) diamagnetic particles in an inertial-FCS device. The experimental data and simulations followed the same trend (Fig. 3b and c). The optimization of the inertial-FCS device provided a collection of optimized operating parameters including the sample flow rate and ferrofluid concentration for cell separation applications. For the specific cell separation reported later in this paper (CTCs and T lymphocytes), we chose the following parameters to maximize the sample processing throughput while reducing the usage of ferrofluids: 0.05% (v/v) ferrofluid concentration and 1000–1200 μL min^{-1} (60–72 mL h^{-1}) flow rate.

Optimization of inertial-ferrohydrodynamic cell separation for high separation resolution

We next optimized the inertial-ferrohydrodynamic cell separation (inertial-FCS) device for high-resolution separation of target cells. We aimed to use the inertial-FCS device to separate cells that had ~1–2 μm difference in their physical diameters. Being able to differentiate cells with such a small diameter difference allowed the device to selectively enrich target cells from contaminating cells that had similar physical morphologies. For this purpose, we first investigated the theoretical separation resolution of the inertial-FCS

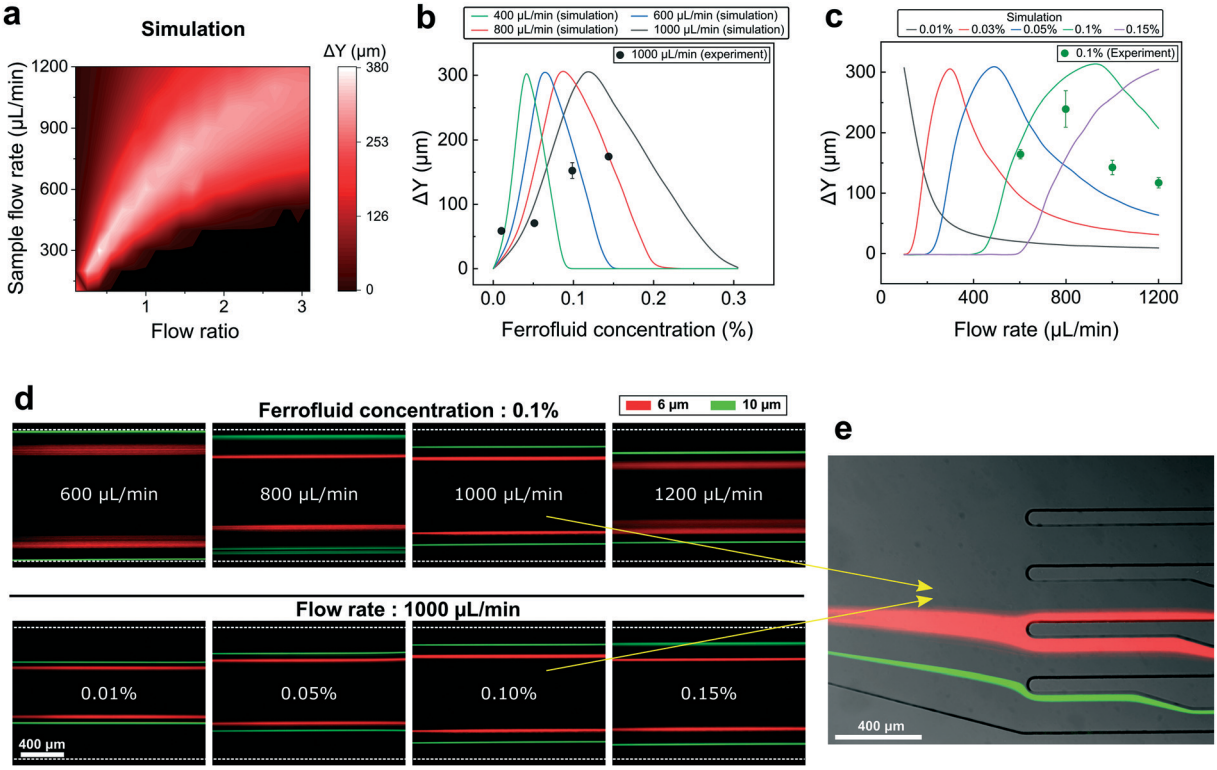

Fig. 3 Optimizations of the inertial-FCS device for high throughput with parameters including the sample/sheath flow ratio, ferrofluid concentration and sample flow rate. (a) Dependence of the diamagnetic particle separation distance (ΔY) on the sample flow rate and the ratio between the sample and sheath flow. We chose a flow ratio of 2 to be able to maintain both the high sample flow rate (~1000 μL min^{-1}) and large separation distance (ΔY) between 6 μm and 10 μm (diameters) diamagnetic particles. (b) Dependence of the separation distance (ΔY) on the ferrofluid concentration (v/v) at variable sample flow rates. The flow ratio between the sample and sheath flow was 2. There was an optimal ferrofluid concentration for each sample flow rate. Based on the application needs, we could choose a combination of a ferrofluid concentration and sample flow rate to maximize the separation distance (ΔY). The black dots represent the experimental separation results of 6 μm and 10 μm (diameters) diamagnetic particles with a sample flow rate of 1000 μL min^{-1} in 0.01%, 0.05%, 0.1%, and 0.15% (v/v) ferrofluids (experimental images in Fig. 3d, bottom panel). (c) Dependence of the separation distance (ΔY) on the sample flow rate at variable ferrofluid concentrations. The flow ratio between the sample and sheath flow was 2. There were optimal sample flow rates for each ferrofluid concentration. The green dots represent the experimental separation results of 6 μm and 10 μm (diameters) diamagnetic particles in 0.1% ferrofluid with sample flow rates of 600, 800, 1000, and 1200 μL min^{-1} (Fig. 3d, top panel). (d) Fluorescence images of particle separation to verify simulation results with different flow rates (top panel, ferrofluid concentration = 0.1%) and different ferrofluid concentrations (bottom panel, flow rate of the sample = 1000 μL min^{-1}). These images were taken at the end of the inertial-FCS device. (e) A fluorescence image showing clear separation of 6 μm (red fluorescence) and 10 μm (green fluorescence) particles at the outlets of the inertial-FCS device. The dashed lines in the fluorescence images indicate the boundaries of the microchannel.

device through simulations, by considering realistic biological samples containing cells with polydisperse physical diameters. We obtained the separation distance between particles that had just 1 μm difference in their diameters, denoted as $\Delta Y_{1\mu m}$, and its dependence on the particle diameter and sample flow rates through simulation as shown in Fig. 4a. The concentration of the ferrofluids was constant at 0.05% (v/v) in this simulation. We chose the separation distance between cells $\Delta Y_{1\mu m}$ to be larger than 100 μm as the criterion for complete separation, because particle streams had finite width even after inertial focusing, and a 100 μm center-to-center distance between particle streams was sufficient for separation based on experimental observations. The main observation from this simulation study (Fig. 4a) was: for particles with a given physical diameter, the optimized sample flow rate leading to complete separation ($\Delta Y_{1\mu m} > 100$ μm) between these particles and smaller/larger particles (1 μm difference in their diameters) depended on the particle diameter. Smaller particles (<10 μm in diameter) required lower flow rates to be separated from each other, while particles of 10–20 μm in diameter required larger flow rates. This observation was expected because as the diameter of particles increased, their volume difference decreased, which made the volume-dependent inertial-FCS method less effective in separating them. Even at high flow rates, the small volume difference between large particles (10–20 μm in diameter, 1 μm in diameter difference) could barely be differentiated by the ferrohydrodynamic force. This finding was validated using fluorescent diamagnetic particles that had well-defined diameters (Fig. 4b), where mixtures of 5 μm and 6 μm, and 6 μm and 7 μm diamagnetic particles were shown to be completely separated at the end of the

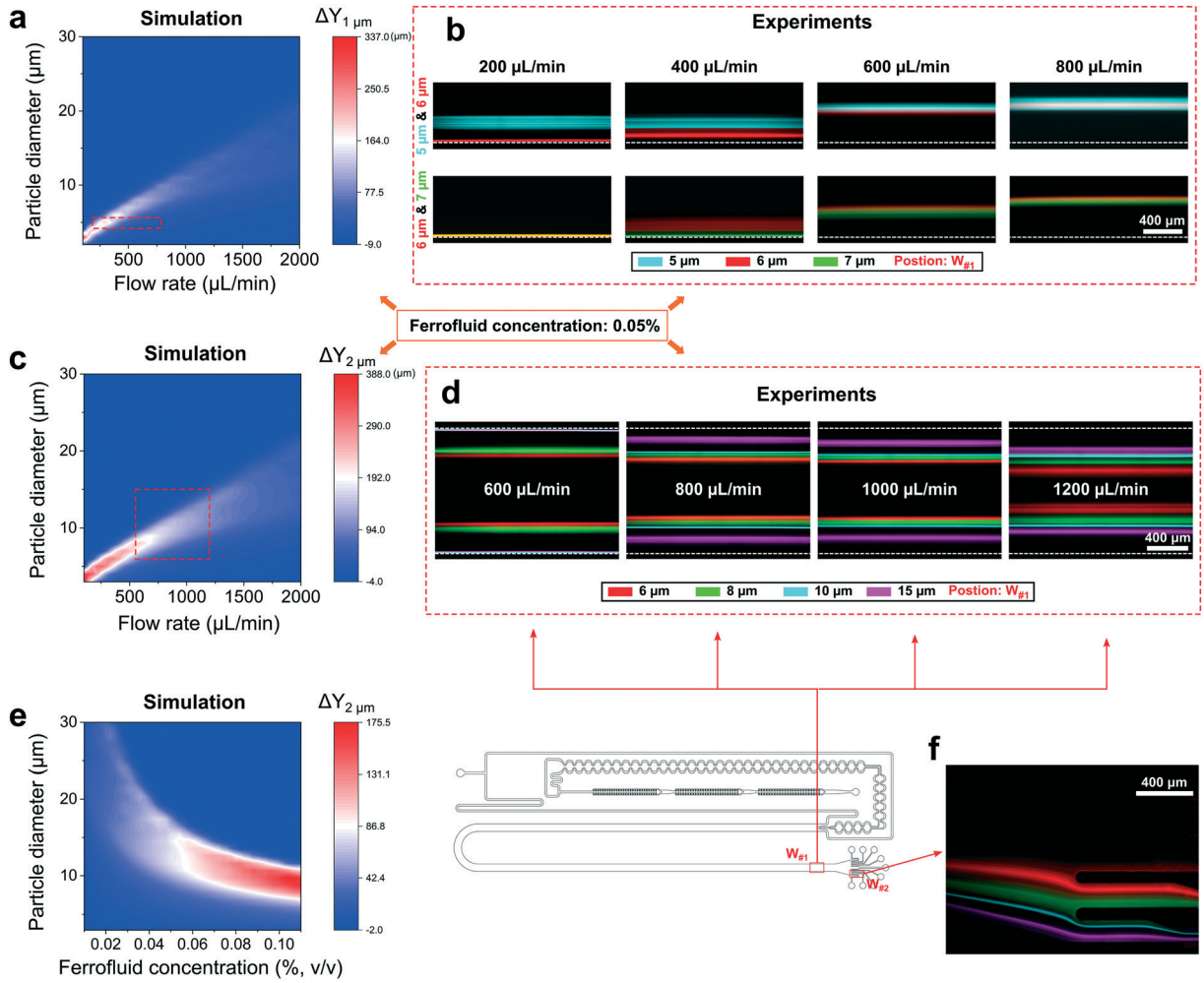

Fig. 4 Optimizations of the inertial-FCS device for high separation resolution with parameters including the ferrofluid concentration and sample flow rate. (a) Simulation results of the separation distance ($\Delta Y_{1\mu m}$) between particles that had 1 μm difference in their physical diameters. $\Delta Y_{1\mu m}$ depended on the flow rate (10–2000 μL min^{-1}) and particle diameter (1–30 μm) at a constant ferrofluid concentration (0.05% (v/v)). (b) Experimental results of separation of 5, 6, and 7 μm (diameters) diamagnetic particles at different flow rates (200, 400, 600, and 800 μL min^{-1}) in a 0.05% (v/v) ferrofluid. Dashed lines in fluorescence images indicate the boundaries of the channel. $W_{\#1}$ indicates the location of the observation window in the device for these fluorescence images. (c) Simulation results of the separation distance ($\Delta Y_{2\mu m}$) between particles that had 2 μm difference in their physical diameters. $\Delta Y_{2\mu m}$ depended on the flow rate (10–2000 μL min^{-1}) and particle diameter (1–30 μm) at a constant ferrofluid concentration (0.05% (v/v)). (d) Experimental results of separation of 6, 8, 10 and 15 μm (diameters) diamagnetic particles at different flow rates (600, 800, 1000, and 1200 μL min^{-1}) in a 0.05% (v/v) ferrofluid. The dashed lines in the fluorescence images indicate the boundaries of the channel. $W_{\#2}$ indicates the location of the observation window in the device for these fluorescence images. (e) Simulation results of the separation distance ($\Delta Y_{2\mu m}$) between particles that had 2 μm difference in their physical diameters. $\Delta Y_{2\mu m}$ depended on the ferrofluid concentration (0.01–0.11% (v/v)) and cell diameter (1–30 μm) at a constant flow rate (1500 μL min^{-1}). (f) Diamagnetic particle (6 μm (red), 8 μm (green), 10 μm (cyan), and 15 μm (purple)) separation at the outlets of the device at a 1000 μL min^{-1} flow rate in a 0.1% (v/v) ferrofluid.

device using optimized flow rates. We concluded that the theoretical separation resolution limit of the inertial-FCS device in particle separation was 1 μm in diameter difference for particles of <10 μm in diameter. For particles of 10–20 μm in diameter, we needed to relax the separation resolution to 2 μm in their diameter difference in order to achieve sufficient separation distance and high sample flow rates. Fig. 4c shows the separation distance $\Delta Y_{2\mu m}$ (separation distance between cells that had 2 μm difference in their diameters) and its dependence on the cell diameter and sample flow rates. The concentration of the ferrofluids was constant at 0.05% (v/v) in this simulation. We noted that a larger separation distance and a higher sample rate could be achieved when separating ($\Delta Y_{2\mu m} > 100$ μm) these particles. Experimentally, we verified this finding by challenging the device with mixtures that consisted of diamagnetic particles with multiple diameters that were close to each other (diameters: 6, 8, 10 and 15 μm). Fig. 4d and f show that these particles were completely separated from each other at very high flow rates (800–1200 μL min^{-1}, or 48–72 mL h^{-1}) at the end of the device. We concluded that the theoretical separation resolution limit of the inertial-FCS device was 2 μm in diameter difference for particles of 10–20 μm in diameter. Both optimizations with

a constant 0.05% (v/v) ferrofluid concentration in Fig. 4a and c indicated that the separation was efficient for particles with diameters less than 20 μm, but less efficient for particles with even larger diameters ($\Delta Y_{1\mu m}$ and $\Delta Y_{2\mu m} \lesssim 100$ μm). To search for parameters that work efficiently for particles of >20 μm in diameter, we simulated the separation distance ($\Delta Y_{2\mu m}$) dependence on the ferrofluid concentration at a constant sample flow rate (1500 μL min^{-1}). Fig. 4e indicates that ferrofluid concentration tuning would allow optimized separation between particles with relatively large diameters. These simulation and experimental studies on the separation resolution of the inertial-FCS device, together with the studies conducted in the previous section, allowed us to determine the optimized sample flow rates, ferrofluid concentration and magnetic field pattern to achieve high-throughput and high-resolution for specific cell separation challenges discussed below.

Validation of inertial-ferrohydrodynamic cell separation with biological samples

After the completion of the inertial-FCS optimizations, we validated the devices in two cell separation applications. The first application was the use of the device in recovering circulating tumor cells from lysed whole blood. The second application was the use of the device in separating lymphocytes from human white blood cells. Due to the large volume of samples and the large quantity of cells, as well as the physical diameter distribution of cells in these samples, we chose sample flow rates of 1000–1200 μL min^{-1} (60–72 mL h^{-1}) and a ferrofluid concentration of 0.05% (v/v) in the inertial-FCS device to achieve high throughput and high separation resolution.

We first conducted the spiked cancer cell validation with the aim of using inertial-FCS devices to recover CTCs from cancer patients' blood. Most CTCs of epithelial origin have a diameter range of 15–25 μm, and are on average larger than other blood components such as red blood cells (RBCs: 6–9 μm in diameter) and the majority of white blood cells (WBCs: 8–14 μm in diameter).[1] However, measurements on the cell diameter of cancer cell lines and WBCs showed that there was a significant diameter overlap between WBCs and cancer cells.[39] There was also a significant percentage of patient-derived CTCs that were smaller than 10 μm in diameter.[39] Because of the polydispersity in the diameter of cancer cells, label-free cancer cell separation methods for CTC applications needed to have a high separation resolution, preferably ~1–2 μm so that target cells could be precisely separated based on their physical diameter while the contamination was minimized. We demonstrated in the spiked cancer cell validation that the inertial-FCS device could separate cancer cells with a resolution of ~2 μm, which led to a high recovery rate and purity of isolated cells. We first used the inertial-FCS device to separate non-small lung cancer cells (H1299) based on their physical diameters. A typical separation process can be visualized in Fig. 5a, in which H1299 lung cancer cells (cell diameter range 3–41 μm) were spiked into 10 mL of ferrofluids (0.05% v/v) and processed in an inertial-FCS device at a flow rate of 72 mL h^{-1}. Cells collected from the outlets of the device showed different mean diameters (Fig. 5b). While the unseparated H1299 cells had a diameter distribution of 14.08 ± 6.47 μm, cells from outlets #1–5 showed much less polydispersity (outlet #1: 20.54 ± 3.34 μm, outlet #2: 13.49 ± 1.23 μm, outlet #3: 10.13 ± 0.99 μm, outlet #4: 8.22 ± 1.26 μm, outlet 5: 3.40 ± 0.92 μm). This confirmed that the inertial-FCS device could separate cancer cells based on their physical diameter and the minimal resolution of the separation was 1.9 μm (between the cells collected from outlets #3 and #4, ESI†). We continued the validation by testing the device with spiked cancer cells in lysed whole blood. A typical separation process can be visualized in Fig. 5c (end of the inertial-FCS device), in which green fluorescently stained H1299 lung cancer cells were spiked into 1 mL of WBCs and processed in a device at a flow rate of 60 mL h^{-1}. The total sample volume was 10 mL and the total number of cells (including cancer cells and WBCs) was ~60 million. The corresponding throughput of the inertial-FCS device for processing these cells was ~100 000 cells per second. We chose the cells that exited from outlet #1 to be the collected cells. Based on our previous studies, cells with a mean physical diameter of 20.54 μm exited *via* outlet #1. This group of cells would include cancer cells as well as large WBCs. Fig. 5c shows that green fluorescent H1299 cells exited predominately through outlet #1. A post-separation analysis of cells from outlet #1 yielded a recovery rate of spiked H1299 cancer cells of 97.2 ± 4.0% and a purity of cancer cells of 9.2 ± 1.1%, at a spike ratio of ~100 cancer cells per one milliliter of blood. We extended the validation to three more cancer cell lines. As shown in Fig. 5d, by using the inertial-FCS method, recovery rates of 91.8 ± 4.3%, 95.4 ± 5.1%, and 94.6 ± 3.1% were obtained for MDA-MB-231 (breast cancer cell line), MCF7 (breast cancer cell line) and H3122 (non-small cell lung cancer cell line), respectively. The average recovery rate across the four cancer cell lines was 94.8%. The average purity of the recovered cancer cells across the four cancer cell lines was 11.0%. We also studied the impact of the inertial-FCS process and the biocompatible ferrofluids on cells. We examined the short-term cell viability, long-term cell proliferation, and morphological changes of cancer cells following the separation process. As shown in Fig. 5e, the cell viability of H1299 cells before and after separation was determined to be 98.3% and 96.2%, respectively, indicating a negligible decrease in cell viability. Representative fluorescence images of cells are shown in Fig. 5f. Fig. 5g shows the images of separated H1299 cells after 48 hours. They were able to proliferate to confluence and maintain their morphology after the separation process. We also compared the morphologies of the cells before and after the inertial-FCS process and observed minimal changes (see the ESI†). In this validation, we demonstrated the ability of inertial-FCS for high-throughput, high-resolution and biocompatible recovery of spiked cancer cells from human white blood cells.

We then validated the inertial-FCS device using blood samples from four stage IIIB/IV lung cancer patients. The patients were recruited from the University Cancer and Blood

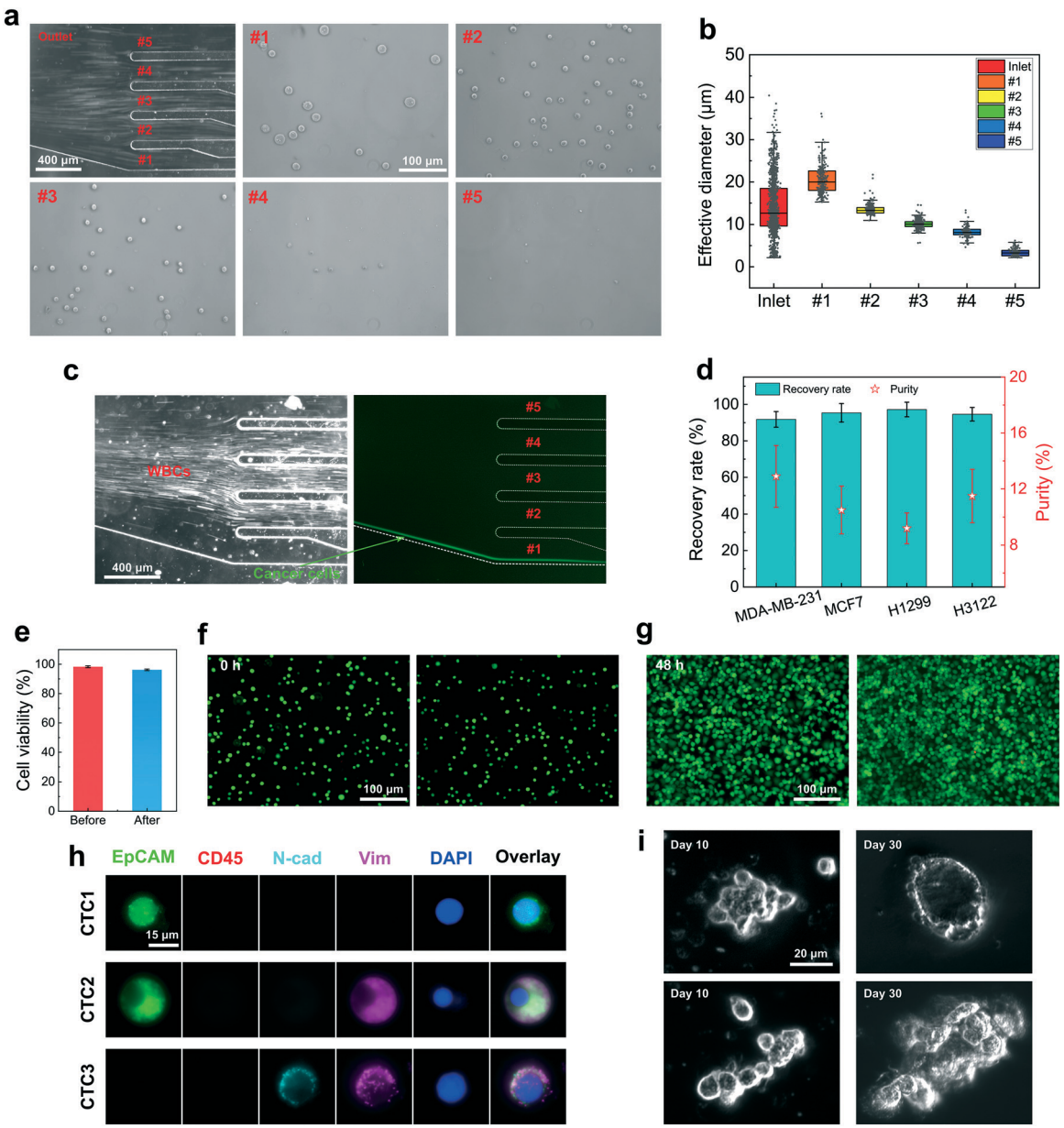

Fig. 5 Inertial-FCS device validation using cancer cells. (a) Bright field images of the separation of H1299 cancer cells based on their physical diameters at the outlets of the inertial-FCS device. ~4×10^5 cancer cells were spiked into 1 mL of 0.05% (v/v) ferrofluid. Cells were collected from the outlets (#1–5) after separation. The cancer cell sample flow rate was 1200 μL min^{-1} (72 mL h^{-1}). (b) Distribution of effective diameters of H1299 cancer cells measured before (inlet) and after (outlets #1–5) the separation. The effective diameters of cancer cells collected from the inlet and outlets #1–5 were 14.08 ± 6.47 μm (n = 1287), 20.54 ± 3.34 μm (n = 246), 13.49 ± 1.23 μm (n = 246), 10.13 ± 0.99 μm (n = 380), 8.22 ± 1.26 μm (n = 134), and 3.40 ± 0.92 μm (n = 118), respectively. (c) Separation of spiked H1299 cancer cells from human white blood cells (left: bright field, phase contrast; right: epifluorescence). ~1000 H1299 cancer cells and 6 million WBCs were spiked into 1 mL of 0.05% (v/v) ferrofluid and processed with a flow rate of 1000 μL min^{-1} (60 mL h^{-1}), and the cell processing throughput was ~100 000 cells per s. Cancer cells stained with CellTracker green were collected from the bottom outlet (#1), while the majority of WBCs were removed from outlets #2–5. (d) Recovery rate and purity of separated cancer cells (~100 cancer cells spiked per 1 mL) for different cancer cells lines at a flow rate of 1000 μL min^{-1} (60 mL h^{-1}). Recovery rates of 91.8 ± 4.3%, 95.4 ± 5.1%, 97.2 ± 4.0%, and 94.6 ± 3.1% were achieved for the MDA-MB-231 (breast cancer), MCF7 (breast cancer), H1299 (lung cancer), and H3122 (lung cancer) cell lines, respectively. The corresponding purities of cancer cells of each cell line were 12.9 ± 2.2% (MDA-MB-231), 10.5 ± 1.7% (MCF7), 9.2 ± 1.1% (H1299), and 11.5 ± 1.9% (H3122), respectively. Error bars indicate standard deviation (s.d.) of experiments (n = 3). (e) Short-term H1299 cancer cell viability comparison before and after the inertial-FCS device processing. The cell viability of the H1299 cancer cell line before and after separation was 98.3 ± 0.7% and 96.2 ± 0.5%, respectively. (f) Fluorescence images of a live/dead assay immediately after H1299 cancer cell separation. Cells were stained with Calcein AM (green, live cells) and EhD-1 (red, dead cells). (g) Representative images of cultured H1299 lung cancer cells after inertial-FCS device processing at 48 hours. The ferrofluid concentration in experiments from (a) to (g) was 0.05% (v/v). (h) Immunofluorescence images of 3 individual CTCs enriched from one stage IV non-small cell lung cancer patient. Five channels were used in immunofluorescence staining, including the epithelial marker EpCAM (green), leukocyte marker CD45 (red), mesenchymal markers N-cadherin (N-cad, cyan) and vimentin (Vim, magenta), and nucleus marker DAPI (blue). CTCs were identified as cells with either epithelial or mesenchymal expression or both while without the leukocyte marker. (i) Bright field images of cultured cells at day 10 and day 30.

Center (Athens, Georgia) and gave informed consent under an approved IRB protocol (University of Georgia, VERSION00000869). Blood was drawn from the patients prior to any cancer related treatment and processed by inertial-FCS devices for CTC separation. After separation, isolated cells were divided for cell identification and cell culture. Cells in the identification portion were stained with an epithelial marker (EpCAM), mesenchymal markers (vimentin and N-cadherin), a leukocyte marker (CD45) and nucleus staining DAPI for their identification. CTCs were identified as epithelial positive (EpCAM+/Vim−/N-cad−/CD45−/DAPI+), mesenchymal positive (EpCAM−/Vim+/CD45−/DAPI+, EpCAM−/N-cad+/CD45−/DAPI+ or EpCAM−/Vim+/N-cad+/CD45−/DAPI+), or both epithelial and mesenchymal positive (EpCAM+/

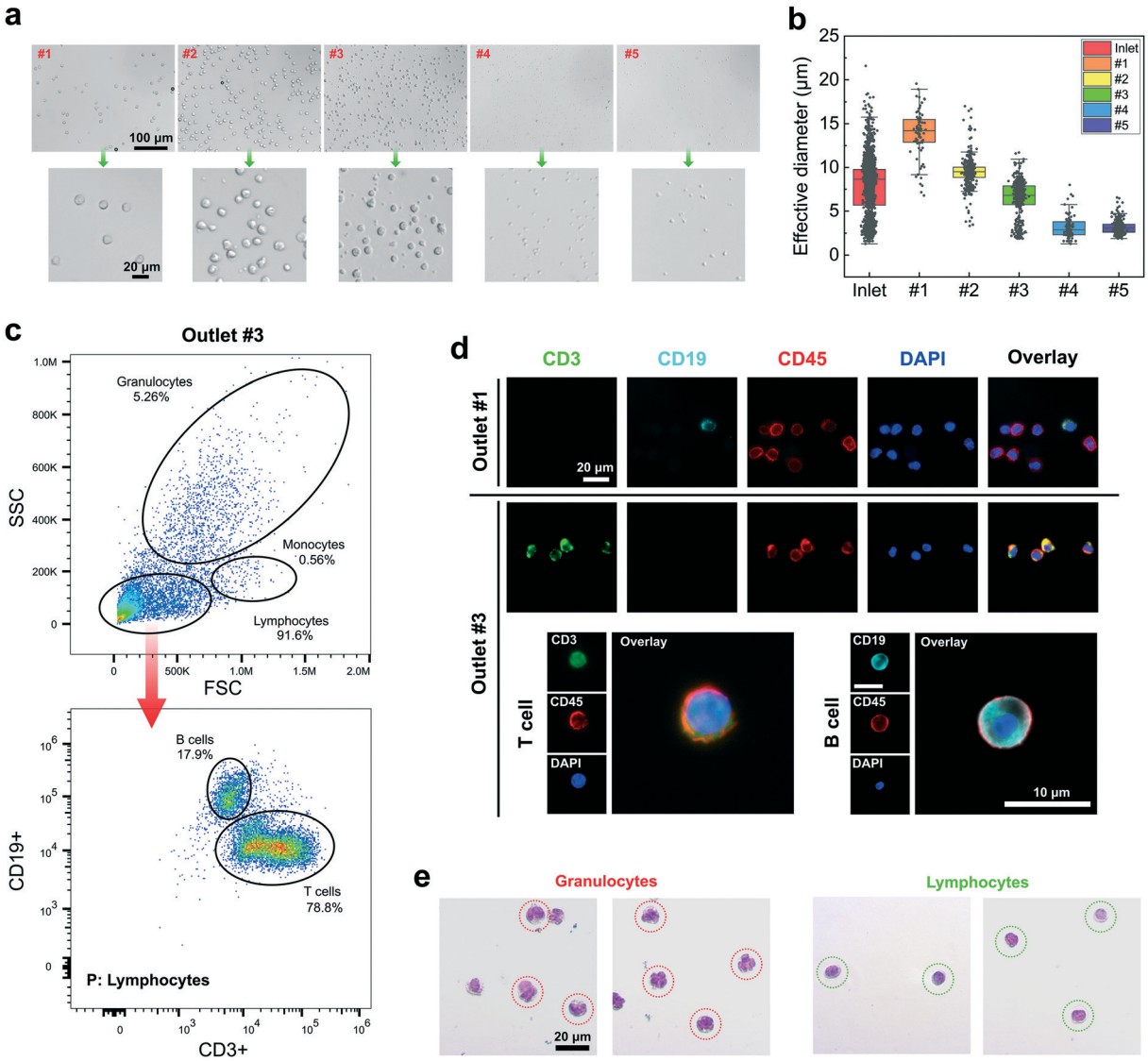

Fig. 6 Inertial-FCS device validation using human white blood cells. (a) Bright field images of the separation of white blood cells based on their physical diameters at the outlets of the inertial-FCS device. Cells were collected from different outlets #1–5 and analyzed for their diameter distribution. The cells were suspended in a 0.05% (v/v) concentration ferrofluid and the cell sample flow rate was 1000 μL min^{-1}. (b) Distribution of effective diameters of cells collected from the inlet (before separation) and outlets #1–5 (after separation). The diameters of cells collected from the inlet and the #1–5 outlets were 7.80 ± 3.14 μm (n = 2585), 13.85 ± 2.67 μm (n = 77), 9.43 ± 1.62 μm (n = 428), 6.39 ± 2.12 μm (n = 442), 3.15 ± 1.27 μm (n = 86), and 3.16 ± 0.77 μm (n = 300), respectively. (c) Flow cytometry results of cells collected from outlet #3 showed that 91.6% of the cells in the outlet #3 collection were lymphocytes, 0.56% were monocytes, and 5.26% were granulocytes (top panel). Lymphocytes collected from outlet #3 included both T lymphocytes and B lymphocytes (bottom panel), which were identified using a combination of CD3 and CD19 antibodies. T lymphocytes were identified as CD3+ and B lymphocytes were identified as CD19+. The lymphocyte population consisted of 78.8% T lymphocytes and 17.9% B lymphocytes. (d) Immunofluorescence images of cells collected from outlets #1 and #3. Four channels were used in the immunofluorescence staining, including the leukocyte marker CD45 (red), T lymphocyte marker CD3 (green), B lymphocyte marker CD19 (cyan), and nucleus marker DAPI (blue). White blood cells were identified as CD45+/DAPI+, while T lymphocytes were determined as CD45+/CD3+/DAPI + and B lymphocytes were determined as CD45+/CD19+/DAPI+. (e) Wright's staining of cells from outlets #1 and #3. Granulocytes collected from outlet #1 are represented by dotted red circles, while lymphocytes collected from outlet #3 are represented by dotted green circles.

Vim+/N-cad+/CD45−/DAPI+), while WBCs were identified as EpCAM−/Vim−/N-cad−/CD45+/DAPI+. The numbers of identified CTCs for all patients are listed in the ESI.† For patient 1, a total of 1452 CTCs were separated from 10 mL of blood from this patient (145 CTCs per mL of blood). Examples of intact CTCs from device outputs are shown in Fig. 5h. Because inertial-FCS allowed us to maintain cell viability and proliferation after separation, we also attempted to culture CTCs after separation for this patient. In our CTC culture protocol, the isolated cells in the culture portion were cultured in DMEM/F12 medium supplemented with B27 supplement, epidermal growth factor, basic fibroblast growth factor, L-glutamine, and penicillin–streptomycin, over a 30 day period. Fig. 5i shows the images of cell clusters at days 10 and 30 of culture. The isolated CTCs remained viable and formed CTC clusters, suggesting that the inertial-FCS devices could potentially isolate viable and expandable CTCs from cancer patients' blood samples. The purities of the CTCs isolated from samples of two patients (patients 3 and 4, ESI†) were 11.70% and 36.39%.

Next we conducted the lymphocyte validation with the aim of using inertial-FCS devices to purify lymphocytes from white blood cells. Lymphocytes consist of B and T cells, which are 6–8 μm in diameter, and larger natural killer cells, which are 12–15 μm in diameter.[40] These lymphocytes co-exist with a large quantity of granulocytes that are 10–15 μm in diameter and monocytes that are 15–30 μm in diameter.[40] We used the inertial-FCS device to separate the lymphocytes from other white blood cells. In this validation, 10 mL lysed human blood with ~60 million WBCs was suspended in a 0.05% (v/v) ferrofluid and processed in the device with a flow rate of 1000 μL min^{-1} (60 mL h^{-1}) and a corresponding throughput of ~100 000 cells per s. After separation, we examined the diameter distributions of cells collected from the device inlet and outlets #1–5. Fig. 6a and b show that the cells from the outlets were significantly less polydisperse than the cells in the inlet (inlet: 7.80 ± 3.14 μm, outlet #1: 13.85 ± 2.67 μm, outlet #2: 9.43 ± 1.62 μm, outlet #3: 6.39 ± 2.12 μm, outlet #4: 3.15 ± 1.27 μm, and outlet #5: 3.16 ± 0.77 μm). We also observed that the platelets with diameters of 2–3 μm were present in outlets #2–5, due to the fact that the inertial focusing stage was less effective in focusing small cells such as platelets (see the ESI†). We collected and analyzed the cells from outlet #3 which had a diameter distribution of 6.39 ± 2.12 μm, because this diameter distribution coincided with the lymphocyte diameter (6–8 μm) reported in the literature.[23,40] The analyses of these cells consisted of flow cytometry for the cell composition and immunofluorescence and hematologic staining for cell differentiation (Fig. 6c–e). From the flow cytometry analysis in Fig. 6c, we found that the cells from outlet #3 primarily consisted of lymphocytes with a small percentage of granulocytes and monocytes (91.6% lymphocytes, 5.26% granulocytes and 0.56% of monocytes, Fig. 6c top panel). The lymphocytes were further revealed to have 78.8% T lymphocytes and 17.9% B lymphocytes (Fig. 6c bottom panel). From the immunofluorescence analysis in Fig. 6d, the lymphocytes recovered from outlet #3 of the device consisted of T lymphocytes (CD3+/CD45+/DAPI+) and B lymphocytes (CD19+/CD45+/DAPI+). Hematologic staining in Fig. 6e also confirmed the presence of lymphocytes in outlet #3. In this validation, we demonstrated the ability of inertial-FCS for high-throughput and high-resolution purification of lymphocytes directly from white blood cells in a label-free manner.

Conclusion

In this study, we reported a label-free inertial-ferrohydrodynamic cell separation (inertial-FCS) method that integrated both inertial focusing and ferrohydrodynamic separation for cell separation based on the physical diameter difference of cells. This method leveraged both the high throughput of the inertial focusing and the high resolution of the ferrohydrodynamic separation to enable rapid and precise cell separation that is urgently needed in fundamental biological research and clinical assays. We performed systematic optimization of the inertial-FCS method and determined operating parameters that enabled it to process more than 60 mL of biological samples within one hour at an extremely high throughput of 100 000 cells per second, a feature that is desired in a variety of biological applications which necessitate processing a large volume of biological samples to search for target cells. The high resolution nature of this method allowed it to differentiate cells with ~1–2 μm difference in their physical diameters, a feature that is critical for label-free and low-cost cell separation applications which often have polydispersed cells with overlapping physical sizes. The inertial-FCS devices could separate spiked cancer cells in a biocompatible manner from white blood cells with high throughput and high resolution. Isolated cancer cells showed a high recovery rate (94.8%) and a high purity (11%), which implied that this method could be used in enriching circulating tumor cells from cancer patients. This was confirmed by using inertial-FCS devices to process blood samples from stage IIIB/IV lung cancer patients. The inertial-FCS devices could also purify lymphocytes directly from white blood cells based on their physical diameters at an extremely high throughput, which could potentially lower the cost associated with adoptive cell transfer therapy because lymphocytes are precursors for potent therapeutic cells. Future optimization of the inertial-FCS method could potentially lead to devices that can process a single blood sample to simultaneously purify both circulating tumor cells and lymphocytes with non-overlapping size profiles.

Materials and methods

Ferrofluid synthesis and characterization

Maghemite nanoparticles (diameter: 10.91 ± 4.86 nm) were synthesized by a chemical co-precipitation method as previously described.[33] The size and morphology of the nanoparticles were characterized using transmission electron microscopy (TEM; FEI, Eindhoven, the Netherlands). The viscosity of the ferrofluid

was measured with a compact rheometer (Anton Paar, Ashland, VA) at room temperature. The volume fraction of the magnetic materials and the saturation magnetization of the ferrofluid were characterized with a vibrating sample magnetometer (VSM: MicroSense, Lowell, MA). In order to achieve biocompatibility, the pH of the ferrofluid was adjusted to 7 and the osmotic pressure was balanced with Hank's balanced salt solution (Thermo Fisher Scientific, Waltham, MA). The concentration of undiluted ferrofluid was measured to be 0.3% (v/v) and the corresponding viscosity of the ferrofluid was 1.68 mPa s at 23 °C.

Cell culture and sample preparation

Cancer cell lines (ATCC, Manassas, VA) including two human breast cancer cell lines (MCF7 and MDA-MB-231), and two human lung cancer cell lines (H1299 and H3122) were used in this study. MCF7 and MDA-MB-231 cells were cultured in DMEM medium (Thermo Fisher Scientific, Waltham, MA), and H1299 and H3122 cells were cultured in RPMI medium. The DMEM and RPMI media were supplemented with 10% (v/v) fetal bovine serum (Thermo Fisher Scientific, Waltham, MA), 1% (v/v) penicillin/streptomycin solution (Thermo Fisher Scientific, Waltham, MA), and 0.1 mM non-essential amino acid solution (Thermo Fisher Scientific, Waltham, MA). The cells were released through incubation with 0.05% trypsin–EDTA solution (Thermo Fisher Scientific, Waltham, MA) at 37 °C for 5 minutes. The concentration of the harvested cells was measured with an automated cell counter (Countess™, Thermo Fisher Scientific, Waltham, MA). After dilution with PBS, the exact number of cells was counted with a Nageotte counting chamber (Hausser Scientific, Horsham, PA). Desired cancer cells were spiked into 1 mL ferrofluid.

Inertial-FCS device fabrication and assembly

The mold of the inertial-FCS device was fabricated using SU-82025 photoresist (Kayaku Advance Materials, Westborough, MA) with a channel height of 60 μm, which was measured with a profilometer (Veeco Instruments, Chadds Ford, PA). Polydimethylsiloxane (PDMS) devices were prepared with a Sylgard 184 silicone elastomer kit (Ellsworth Adhesives, Germantown, WI) using a 1 : 7 ratio of a cross linker and base, followed by curing at 70 °C for 3 hours. The fabricated microchannel was placed in a sextupole permanent magnet array (N52, K&J Magnetics, Pipersville, PA) and held in a custom-made aluminum manifold. Each magnet was 50.8 mm in length and 6.35 mm in both width and thickness, with a residual magnetic flux density of 1.48 T.

Microfluidic experimental setup and procedure

The inertial-FCS microchannel was first treated with plasma for 3 minutes, followed by ethanol (70%) flushing for 10 minutes. The microchannel was then primed with PBS supplemented with 0.5% (w/v) bovine serum albumin (BSA) and 2 mM EDTA (Thermo Fisher Scientific, Waltham, MA). Sample fluids and sheath fluids were individually controlled with syringe pumps (Chemyx, Stafford, TX) at variable flow rates. Images and videos of cells were obtained with an inverted microscope equipped with a CCD camera (Carl Zeiss, Germany).

CTC processing

Cancer patient samples collected at the University Cancer and Blood Center (Athens, Georgia) were approved by the University of Georgia Institutional Review Board (IRB) (VERSION00000869) before study initiation and informed consent was obtained from the participants. Blood was first lysed with RBC lysis buffer (eBioscience, San Diego, CA) for 10 minutes at room temperature, centrifuged at 500*g* for 5 minutes, and resuspended in 0.05% ferrofluid. After processing with the inertial-FCS device, the collected cells were centrifuged at 500*g* for 5 minutes at room temperature and resuspended in DMEM/F12 medium supplemented with B27 supplement (1×; Thermo Fisher Scientific, Waltham, MA), epidermal growth factor (20 ng mL^{-1}; Millipore Sigma, Burlington, MA), basic fibroblast growth factor (10 ng mL^{-1}; Thermo Fisher Scientific, Waltham, MA), L-glutamine (2 mM; Thermo Fisher Scientific, Waltham, MA), and penicillin–streptomycin (1×; Thermo Fisher Scientific, Waltham, MA). Cells were cultured in a vented T25 flask at 37 °C with 5% CO_2. Cultures were supplemented with fresh medium every 3 days and washed every 5 days with 1× PBS.

Human white blood cells

Human whole blood cells from donors were purchased from a commercial source (Zen-Bio, Research Triangle, NC) and lysed with RBC lysis buffer (eBioscience, San Diego, CA) for 5 minutes to remove red blood cells at room temperature. The remaining blood cells were then suspended in the same volume of ferrofluid (0.05% v/v) containing 0.1% (v/v) Pluronic F-68 non-ionic surfactant (Thermo Fisher Scientific, Waltham, MA) before device processing.

Flow cytometry of WBCs

Types of separated WBCs were confirmed using flow cytometry (Agilent Quanteon, Agilent, Santa Clara, CA). The WBC size and granularity were used to distinguish the granulocytes, lymphocytes and monocytes. Size information was collected from the forward scatter (FSC) while the granularity of the cells was predicted with the side scatter. Fluorescence signals were used to further identify the WBC types: CD45+/CD3+ was classified as T lymphocytes; CD45+/CD19+ was classified as B lymphocytes.

Immunofluorescence staining

After inertial-FCS device processing, all the outlet samples were collected and resuspended with PBS. The collected cells were fixed with 4% (w/v) paraformaldehyde solution (Santa Cruz Biotechnology, Inc., Dallas, TX) for 10 minutes and subsequently

permeabilized with 0.1% (v/v) Triton X-100 (Alfa Aesar, Haverhill, MA) in PBS for 10 minutes. The cells were blocked with a blocking reagent (Santa Cruz Biotechnology, Dallas, TX) for 30 minutes to reduce non-specific binding, and immunostained with primary antibodies. In the CTC experiments, the primary antibodies used were anti-EpCAM, anti-CD45, anti-vimentin, and anti-N-cadherin (Santa Cruz Biotechnology, Inc, Dallas, TX). Anti-CD45, anti-CD3, and anti-CD19 (Santa Cruz Biotechnology, Inc, Dallas, TX) were used in the lymphocyte experiments. After immunofluorescence staining, the cells were washed and resuspended with PBS. A small portion of cells was coverslipped with mounting medium supplied with DAPI (Electron Microscopy Sciences, Hatfield, PA) for imaging.

Hematologic staining of WBCs

Separated WBCs were differentiated using Wright's stain (Millipore Sigma, Burlington, MA) following the manufacturer's protocol. Briefly, the isolated cells were placed on poly-L-lysine coated glass slides for 1 hour at 4 °C. The slides were flooded with 1 mL Wright's stain. After 30 seconds, 1 mL deionized water was added and mixed thoroughly for 1 minute. The slides were thoroughly rinsed with deionized water and air-dried before inspection and imaging.

Cancer cell recovery rate and purity calculation

The collected cells from the device outlets were stained with 2 μM DAPI (Thermo Fisher Scientific, Waltham, MA) to identify the nucleated cells. The number of cells was counted with a Nageotte counting chamber. Cells with a CellTracker signal were identified as cancer cells, while other cells with a DAPI signal were classified as white blood cells. The recovery rate was calculated by the number of collected cancer cells/the number of spiked cancer cells. The purity was calculated by the number of collected cancer cells/the number of collected nucleated cells.

Cell diameter measurement

Cells were deposited onto microscope slides and imaged with a microscope in bright field mode. The images of the cells were analyzed using the ImageJ software. The effective diameter of the cells was calculated using their surface areas with the assumption that the cells were spherical.

Conflicts of interest

Inertial-FCS is the subject of the United States utility patent application 63/145391. Intellectual property related to inertial-FCS is owned by the University of Georgia Research Foundation. Leidong Mao founded and owned FCS Technology LLC to commercialize inertial-FCS. Wujun Zhao has a financial interest in FCS Technology LLC. Leidong Mao has a financial interest in FCS Technology LLC, which is subject to certain restrictions under the university policy. The terms of this arrangement are being managed by the University of Georgia in accordance with its conflict of interest policies.

Acknowledgements

We thank the Cytometry Shared Resource Laboratory at the Center for Tropical and Emerging Global Diseases at the University of Georgia for their assistance in the flow cytometry analysis. We are extremely grateful to the donors of blood samples for this study. This study is supported by the National Science Foundation under Grant No. 1150042, 1659525 and 1648035, the National Center for Advancing Translational Sciences of the National Institutes of Health under Award No. UL1TR002378, and the National Institute of Biomedical Imaging and Bioengineering of the National Institutes of Health under Award No. 1R41EB028191-01. The content is solely the responsibility of the authors and does not necessarily represent the official views of the National Institutes of Health.

References

1 Y. Chen, P. Li, P. H. Huang, Y. Xie, J. D. Mai, L. Wang, N. T. Nguyen and T. J. Huang, *Lab Chip*, 2014, **14**, 626–645.
2 C. W. t. Shields, C. D. Reyes and G. P. Lopez, *Lab Chip*, 2015, **15**, 1230–1249.
3 D. R. Gossett, W. M. Weaver, A. J. Mach, S. C. Hur, H. T. Tse, W. Lee, H. Amini and D. Di Carlo, *Anal. Bioanal. Chem.*, 2010, **397**, 3249–3267.
4 M. Poudineh, E. H. Sargent, K. Pantel and S. O. Kelley, *Nat. Biomed. Eng.*, 2018, **2**, 72–84.
5 C. Alix-Panabieres and K. Pantel, *Nat. Biomed. Eng.*, 2017, **1**, 1–3.
6 J. Massague and A. C. Obenauf, *Nature*, 2016, **529**, 298–306.
7 M. G. Krebs, R. L. Metcalf, L. Carter, G. Brady, F. H. Blackhall and C. Dive, *Nat. Rev. Clin. Oncol.*, 2014, **11**, 129–144.
8 E. Heitzer, I. S. Haque, C. E. S. Roberts and M. R. Speicher, *Nat. Rev. Genet.*, 2019, **20**, 71–88.
9 N. Ma and S. S. Jeffrey, *Science*, 2020, **367**, 1424–1425.
10 C. H. June, R. S. O'Connor, O. U. Kawalekar, S. Ghassemi and M. C. Milone, *Science*, 2018, **359**, 1361–1365.
11 S. A. Rosenberg and N. P. Restifo, *Science*, 2015, **348**, 62–68.
12 S. A. Rosenberg, *Nat. Rev. Clin. Oncol.*, 2014, **11**, 630–632.
13 B. P. Dodson and A. D. Levine, *BMC Biotechnol.*, 2015, **15**, 70.
14 S. Miltenyi, W. Muller, W. Weichel and A. Radbruch, *Cytometry*, 1990, **11**, 231–238.
15 W. A. Bonner, H. R. Hulett, R. G. Sweet and L. A. Herzenberg, *Rev. Sci. Instrum.*, 1972, **43**, 404–409.
16 K. K. Zeming, N. V. Thakor, Y. Zhang and C.-H. Chen, *Lab Chip*, 2016, **16**, 75–85.
17 P. Li, Z. M. Mao, Z. L. Peng, L. L. Zhou, Y. C. Chen, P. H. Huang, C. I. Truica, J. J. Drabick, W. S. El-Deiry, M. Dao, S. Suresh and T. J. Huang, *Proc. Natl. Acad. Sci. U. S. A.*, 2015, **112**, 4970–4975.
18 Y.-C. Kung, K. R. Niazi and P.-Y. Chiou, *Lab Chip*, 2021, **21**, 1049–1060.
19 J. Takagi, M. Yamada, M. Yasuda and M. Seki, *Lab Chip*, 2005, **5**, 778–784.
20 J. Darabi and C. Guo, *Biomicrofluidics*, 2013, **7**, 054106.

21 M. Mizuno, M. Yamada, R. Mitamura, K. Ike, K. Toyama and M. Seki, *Anal. Chem.*, 2013, **85**, 7666–7673.
22 M. E. Warkiani, B. L. Khoo, L. Wu, A. K. P. Tay, A. A. S. Bhagat, J. Han and C. T. Lim, *Nat. Protoc.*, 2016, **11**, 134–148.
23 P. L. Chiu, C. H. Chang, Y. L. Lin, P. H. Tsou and B. R. R. Li, *Sci. Rep.*, 2019, **9**, 1–10.
24 N. Nivedita and I. Papautsky, *Biomicrofluidics*, 2013, **7**, 054101.
25 E. Sollier, D. E. Go, J. Che, D. R. Gossett, S. O'Byrne, W. M. Weaver, N. Kummer, M. Rettig, J. Goldman, N. Nickols, S. McCloskey, R. P. Kulkarni and D. Di Carlo, *Lab Chip*, 2014, **14**, 63–77.
26 Z. Wu, Y. Chen, M. Wang and A. J. Chung, *Lab Chip*, 2016, **16**, 532–542.
27 J. Cruz, T. Graells, M. Walldén and K. Hjort, *Lab Chip*, 2019, **19**, 1257–1266.
28 D. Di Carlo, D. Irimia, R. G. Tompkins and M. Toner, *Proc. Natl. Acad. Sci. U. S. A.*, 2007, **104**, 18892–18897.
29 H. Amini, W. Lee and D. Di Carlo, *Lab Chip*, 2014, **14**, 2739–2761.
30 D. Di Carlo, *Lab Chip*, 2009, **9**, 3038–3046.
31 R. E. Rosensweig, *Ferrohydrodynamics*, Cambridge University Press, Cambridge, 1985.
32 W. Zhao, R. Cheng, B. D. Jenkins, T. Zhu, N. E. Okonkwo, C. E. Jones, M. B. Davis, S. K. Kavuri, Z. Hao, C. Schroeder and L. Mao, *Lab Chip*, 2017, **17**, 3097–3111.
33 W. Zhao, R. Cheng, S. H. Lim, J. R. Miller, W. Zhang, W. Tang, J. Xie and L. Mao, *Lab Chip*, 2017, **17**, 2243–2255.
34 W. Zhao, T. Zhu, R. Cheng, Y. Liu, J. He, H. Qiu, L. Wang, T. Nagy, T. D. Querec, E. R. Unger and L. Mao, *Adv. Funct. Mater.*, 2016, **26**, 3990–3998.
35 W. Zhao, R. Cheng, J. R. Miller and L. Mao, *Adv. Funct. Mater.*, 2016, **26**, 3916–3932.
36 X. Xuan, *Micromachines*, 2019, **10**, 744.
37 R. Cheng, T. Zhu and L. Mao, *Microfluid. Nanofluid.*, 2014, **16**, 1143–1154.
38 T. Zhu, D. J. Lichlyter, M. A. Haidekker and L. Mao, *Microfluid. Nanofluid.*, 2011, **10**, 1233–1245.
39 W. Zhao, Y. Liu, B. D. Jenkins, R. Cheng, B. N. Harris, W. Zhang, J. Xie, J. R. Murrow, J. Hodgson, M. Egan, A. Bankey, P. G. Nikolinakos, H. Y. Ali, K. Meichner, L. A. Newman, M. B. Davis and L. Mao, *Lab Chip*, 2019, **19**, 1860–1876.
40 P. R. Wheater, H. G. Burkitt and V. G. Daniels, *Functional histology: A text and colour atlas*, Churchill Livingstone, 1979.

